# Deterministic Point Cloud Registration via Novel Transformation Decomposition (Supplementary Material)

Wen Chen[1,*] Haoang Li[1,*] Qiang Nie[1,2] Yun-Hui Liu[1,†]
[1]The Chinese University of Hong Kong, Hong Kong, China
[2]Tencent Youtu Lab, Shenzhen, China

## Overview

In the supplementary material, we provide additional contents that are not included in the main paper due to the space limit:

- Proof of the Lemma 3.1 (see Section 1).
- Discussion about optimality of our two-stage search strategy by taking a multi-line fitting with constraints problem for example (see Section 2).
- Introduction of different methods to discretize the parameter space of the rotation axis (see Section 3).
- Additional comparisons between our TR-DE and state-of-the-art methods on real-world datasets (see Section 4).
- Additional experiments of the proposed method on the purely rotational registration problem (see Section 5). Experiments show that our method achieves better efficiency while keeping high accuracy and good robustness, compared with state-of-the-art rotation estimation approaches.

## 1. Proof of Lemma 3.1

The Lemma 3.1 is the basis of our transformation decomposition. We present the proof of the Lemma 3.1 in our paper as follows.

*Proof.* For any rotation angle $\theta \in [\pi, \pi]$ around a fixed rotation axis $\mathbf{r}$, the point $\mathbf{Rx}$ has a fixed relative angle $\gamma$ with the axis $\mathbf{r}$. Since the rotation operation does not change the length, i.e. $\|\mathbf{Rx}\| = \|\mathbf{x}\|$. $\mathbf{Rx}$ lies on a circle perpendicular to the axis $\mathbf{r}$, shown in Fig. 1. Thus, the projections of $\mathbf{r}$ over $\mathbf{Rx}$ and $\mathbf{x}$ have same length $L$. Hence by the dot product, we have

$$\mathbf{r}^\top (\mathbf{Rx}) = L \cdot \|\mathbf{Rx}\| = L \cdot \|\mathbf{x}\| = \mathbf{r}^\top \mathbf{x}.$$

□

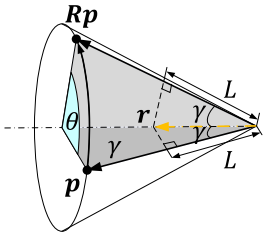


Figure 1. Illustration of the geometrical relationship between $\mathbf{Rx}$ and $\mathbf{x}$, and the projection of the rotation axis on them.

## 2. Multi-line Fitting with Constraints

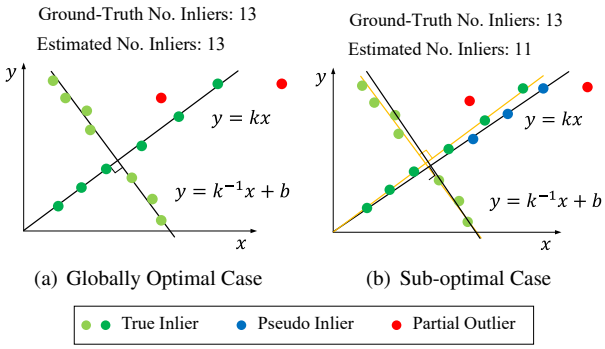


(a) Globally Optimal Case (b) Sub-optimal Case

Figure 2. Illustration of performing the two-stage search to obtain the 2-DOF optimal orthogonal lines fitting most inliers from a group of points corrupted by noise and outliers. (a) We first search for $k$, i.e. the slope of the line pass through the origin. Then, by fixing k, we search for $d$, i.e, the intercept of the second line. The optimal $k$ and $d$ fit all true lines. (b) If there are pseudo inliers in the first-stage search, we may discard some true inliers and contain pseudo inliers by mistake. Then in the second-stage search, more true inliers may be discarded. The two-stage search strategy may fail to provide optimal results.

In our two-stage search strategy, we sequentially search for the parts of the DOF. Ideally, in the first stage, we can retain all true inliers and some pseudo inliers (both of them are our candidate inliers). Then, in the second stage, all the pseudo inliers can be pruned, and all the true inliers are still

*Wen Chen and Haoang Li contributed equally to this work.
†Yun-Hui Liu is corresponding author.

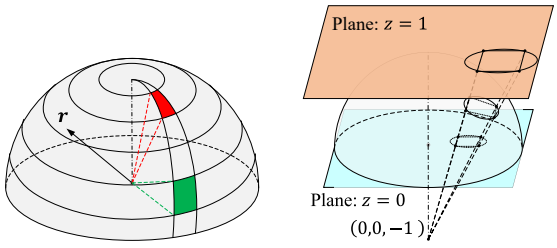


(a) Spherical Mapping (b) Stereographic Projection

Figure 3. Illustration of the discretization of the hemisphere space. (a) The spherical mapping: the red and blue faces have equal relative angles on the latitude axis, but have different areas. (b) The stereographic projection: it projects a hemisphere to a disk in plane $z = 0$ or $z = 1$ and preserves the local shape.

kept. However, in practice, this ideal performance cannot be achieved in all cases. To facilitate understanding of the optimality discussion, we take a multi-line fitting with constraints for example. Similar with our point cloud problem, searching for parameters of the multi-line fitting problem can be decomposed into two sequential search stages. The details are shown as follows.

As shown in Fig. 2(a), there are two straight lines satisfying two constraints: the first one passes through the origin, i.e. the equation is $y = kx$ where $k$ is the unknown slope; the second line is orthogonal to the first one, i.e. the equation is $y = k^{-1}x + b$ where $b$ is the unknown intercept. These two lines have 2 DOF: the slope of the first line ($k$) and the intercept of the second line ($d$). We aim to search for $k$ and $d$ maximizing the number of points on these two lines (up to an inlier threshold, represented as radii of the solid circle in Fig. 2). In the case of Fig. 2(a), we can first find $k$ such that the first line pass through 5 points at most. Then we fix $k$ and search for $d$ such that the second line can fit 7 points. Thus, the number of estimated inliers is equal to the ground-truth. However, in the case of Fig. 2(b), there are 3 blue points very close to the optimal line, which will make some trouble for our first-stage searching for $k$. The first line can fit the maximum number of points only when it passes through these three blue points and discards two true inliers (the two deep green point close to the blue ones). Due to the "greed" in the first stage, we can only search for $d$ such that the second line fits 4 points. As a result, the final number of inliers is less than the ground-truth. But from another perspective, this two-stage search strategy can find a relatively good sub-optimal solution.

## 3. Discretization of Space of Rotation Axis

We model the parameter space of the rotation axis $\mathbf{r}$ by a unit hemisphere. To facilitate our BnB-based search estimation of rotation axis, we need to discretize the hemisphere. The longitude-latitude representation, namely the spherical mapping, is a commonly used method to discretize the sphere. As shown in Fig. 3(a), the equi-angular discretization on the latitude axis leads to faces with different areas. The inconsistency may affect the convergence of BnB-based search methods. Inspired by [9] and [12], we introduce different projection methods to discretize the hemisphere with 2D coordinates. As shown in Table 1, we choose three representative projections with different properties[1]: stereographic projection (conformal, see Fig. 3(b)), Behrmann projection (equal-area), and Miller projection (compromise). Note that, there is no suitable geometrical construction of the Miller projection and Behrmann projection. Interested readers can refer to [12] for the detailed mathematical formulations for these projection methods. In Section 5.1, we compare their performance on the task of the BnB-based searching for the rotation axis. We perform branching operations on these 2D spaces (see Table. 1) and back-project the sub-spaces onto the hemisphere for computing bounds. By the experimental evaluation, the Miller projection outperforms other methods in terms of efficiency, while having comparable accuracy.

Table 1. 2D coordinates for discretization of the hemisphere.

| Projections | 2D coordinates | Shape |
|---|---|---|
| Spherical | $\alpha \in [-\pi, \pi], \beta \in [0, \pi/2]$ | Rectangle |
| Stereographic | $\lambda \in [0, 2], \gamma \in [-\pi, \pi]$ | Disk |
| Behrmann | $x \in [-\frac{\sqrt{3}\pi}{2}, \frac{\sqrt{3}\pi}{2}], y \in \left[0, \frac{2}{\sqrt{3}}\right]$ | Rectangle |
| Miller | $x \in [-\pi, \pi], y \in [0, \frac{5}{4}\ln(\tan\frac{9\pi}{20})]$ | Rectangle |

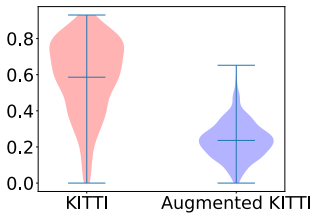


Figure 4. Illustration of the distribution of the inlier ratios for all point cloud pairs in KITTI and Augmented KITTI.

## 4. Additional Results

We first report the detailed scene-wise registration results of our method on the 3DMatch dataset in Table 2. *IP* and *IR* represent the inlier precision and recall respectively. Next, we show additional results on the KITTI dataset.

As shown in Fig. 4, the average inlier ratio (ground-truth) of the putative correpondences generated by FCGF is $58.7\%$. With these "nearly saturated" correspondences as input, almost all methods have satisfactory results. In order to make a more complete comparison, we apply data augmentation on the KITTI dataset by adding random rota-

[1] *Conformal* indicates the projection preserves local shape, *equal-area* implies that area is conserved everywhere, and *compromise* achieves the balance between conformal and equal-area to reduce overall distortion.

Table 2. Scene-wise statistics for TR-DE on 3DMatch.

| | *SR* (%) | *RE* (°) | *TE* (cm) | *IP* (%) | *IR* (%) | $F1$ (%) |
|---|---|---|---|---|---|---|
| Kitchen | 97.23 | 1.82 | 4.5 | 91.98 | 97.22 | 94.12 |
| Home1 | 94.23 | 1.56 | 5.09 | 95.25 | 98.23 | 96.6 |
| Home2 | 86.54 | 2.18 | 8.4 | 95.69 | 98.08 | 96.66 |
| Hotel1 | 96.9 | 1.68 | 5.94 | 94.57 | 97.9 | 96.04 |
| Hotel2 | 87.5 | 1.69 | 6.38 | 96.82 | 98.34 | 96.99 |
| Hotel3 | 94.44 | 1.47 | 4.43 | 97.77 | 98.71 | 98.22 |
| Study | 89.73 | 2.13 | 8.2 | 94.85 | 97.41 | 95.93 |
| Lab | 87.01 | 1.73 | 6.73 | 92.72 | 95.64 | 93.69 |

Table 3. Registration results on the augmented KITTI dataset using FCGF features.

| | *SR* (%) | *RE* (°) | *TE* (cm) | $F1$(%) | Time (s) |
|---|---|---|---|---|---|
| FGR [17] | 80 | 0.4 | 28.58 | - | 0.16 |
| TEASER [15] | 84.68 | 0.33 | 23.88 | 69.46 | 2.27 |
| RANSAC1k [7] | 69.37 | 1.07 | 31.13 | 56.6 | **0.03** |
| RANSAC10k | 83.06 | 0.66 | 26.93 | 69.06 | 0.22 |
| PointDSC [1] | 83.6 | **0.32** | 22.67 | 71.18 | 0.1 |
| **TR-DE (ours)** | **85.59** | 0.33 | **18.67** | **75.29** | 1.25 |

tion and translation. We extract FCGF features from these augmented point clouds. The average inlier ratio (ground-truth) of the augmented KITTI is then reduced to $23.6\%$. As shown in Table 3, our method achieves better performance in terms of *SR*, *TE* and $F1$. And our method is relatively more efficient than the existing deterministic method (*TEASER*).

# 5. Purely Rotational Registration

In this section, we consider the special cases of point cloud registration with known translation or purely rotational motion. Note that, the case of known translation can be transfer to the case of purely rotational motion by transforming the target point cloud with the translation before estimating rotation. The purely rotational registration is also known as the Wahba problem [14] or rotation search problem [5, 4]. In addition to the point cloud registration [11, 3], this type of problem finds extensive applications in image stitching [2] and vanishing point estimation [8].

We extend our method to solve the problem by setting all variables associated with the known translation as zeros. Accordingly, the search spaces of stages I and II are reduced from (2+1)-DOF and (1+2)-DOF spaces to 2-DOF rotation axis and 1-DOF rotation angle respectively. We compare our method with state-of-the-art approaches on the synthetic and real-world datasets. Extensive experiments show that our method achieves better efficiency while keeping high accuracy and good robustness, compared with state-of-the-art approaches.

The experiments are organized as follows. First, we compare the performance of the rotation axis estimation with different discretization methods in Section 5.1. Next, we compare our method with the state-of-the-art algorithms on real-world datasets in Section 5.2. Finally, we show the application of our method in the image stitching problem (see Section 5.3).

## 5.1. Evaluation on Synthetic Dataset

**Data Generation.** We synthesize a set of $N$ points in the cube $[-0.5, 0.5]^3$ as the source point cloud. Moreover, we add zero-mean Gaussian noise whose standard deviation is denoted by $\sigma$ on each point. We produce the target point cloud by moving the source point cloud with a random rotation. Putative correspondences are determined by the index of the points. We denote outlier ratio by $\rho$. The outlier correspondences are generated by randomly choosing $\rho N$ points from the target point cloud and adding random vectors on these outlier points. In the following experiments, we will assign different values of $N$, $\sigma$, and $\rho$ for different comparisons.

**Evaluation Metric.** To evaluating the performance of the estimation of rotation axis $\mathbf{r}$, we introduce the error metric: rotation axis error $e_{\mathbf{r}}$. Mathematically, it is defined as

$$e_{\mathbf{r}} = \arccos\left(|\mathbf{r}_{es} \cdot \mathbf{r}_{gt}|\right) \tag{1}$$

where $(\cdot)_{es}$ and $(\cdot)_{gt}$ represent estimated results and ground-truth values respectively.

**Comparisons of Discretization Methods.** We compare the influence of these discretization methods on the performance of the BnB-based searching for rotation axis. Four methods are aforementioned in Section 3, including the spherical mapping (Sph), stereographic projection with projection plane at $z = 1$ (Ste1), Behrmann projection (Beh), and Miller projection (Mil). The other two methods are introduced in [9], stereographic projection with projection plane at $z = 0$ (Ste2) and exponential mapping (Exp).

The parameters of the synthetic datasets are: $N = 500$, $\delta = 0.005$ and $\rho = 50\%$. We generate the rotation axes $\mathbf{r}_{gt}$ by evenly sampling $16000$ unit vectors on the hemisphere. The rotation angle is fixed as $45°$ such that $16000$ rotations and associated target point clouds are produced. Figs. 7(a) and 7(b) respectively show the histogram statistics of the convergence runtimes and rotation axis errors of the searching for $\mathbf{r}$ with these discretization methods. The Behrmann projection has the worst performance in our settings, because it has more cases of runtime $> 50\ ms$ or error $> 0.9°$. In contrast, the Miller projection achieves the best performance in terms of efficiency while having competitive accuracy.

**Robustness of Rotation Axis Estimation.** In this test, we aim to evaluate the robustness to noise and outliers of the rotation axis estimation with six discretization methods. The number of points $N$ is set as 500. To evaluate the robustness to noise, we set $\sigma$ ranging from $0.005$ to $0.05$ with fixed $\rho = 50\%$. On the other hand, the outlier ratio is set from $15\%$ to $95\%$ with fixed noise $\sigma = 0.005$ for evaluating the

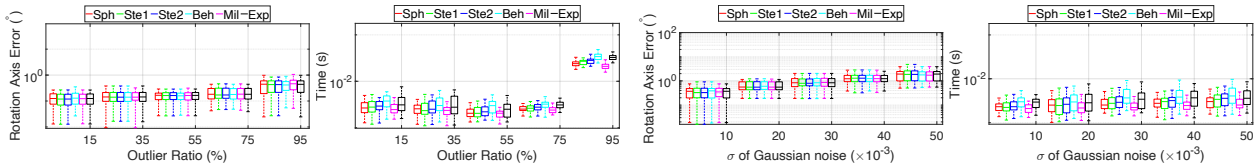


(a) (Error / time) vs. (outlier ratio) for the rotation axis estimation. (b) (Error / time) vs. (noise) for the rotation axis estimation.

Figure 5. Robustness comparisons with respect to the outlier ratio and Gaussian noise for evaluating the performance of the rotation axis search methods based on different discretization.

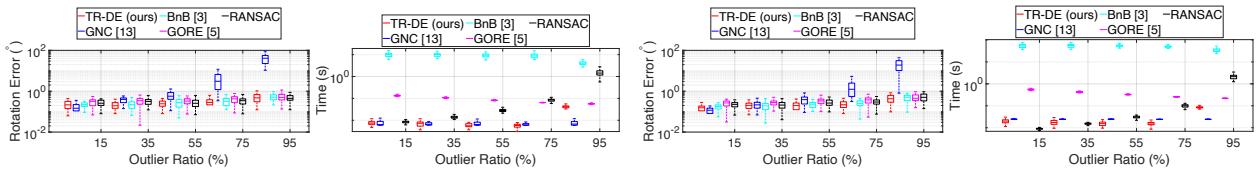


(a) Rotation estimation ($N = 1000$). (b) Rotation estimation ($N = 2000$).

Figure 6. Robustness comparisons with respect to the outlier ratio. Each box-plot is the statistics of estimation on 500 independent trials. Results show that our method outperforms other methods in terms of efficiency while keeping competitive accuracy and robustness.

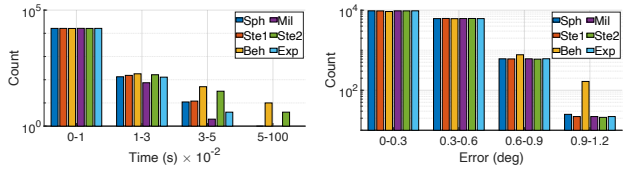


(a) Statistics of runtime. (b) Statistics of axis error.

Figure 7. The histogram statistics of the convergence time and error for six discretization methods on the whole hemisphere.

robustness to outliers. Under each $\sigma$ or $\rho$, 500 independent trials with random rotations are conducted.

Figs. 5(a) and 5(b) report the performance of the rotation axis estimation on point-sets with increasing outlier ratios and noises. From Fig. 5(a), the BnB-based search for rotation axis with all six discretization methods is generally robust against outliers. Even for the cases with high outlier ratios (95%), the algorithms can also converge to a relatively good result in a very short time. The results of experiments on varying noises are presented in Fig. 5(b). As expected, regardless of the increasing noise level and outlier ratio, the BnB-based search with the Mil discretization achieves the most efficient performance among all the tests while having competitive accuracy compared with other methods.

## 5.2. Evaluation on Real-world Dataset

**Data Preparation.** In this section, we compare the proposed *RO-DE* with the state-of-the-art rotational registration techniques on real-world dataset. Following [15], we use the Bunny model from the Stanford 3D Scanning Repository [6]. We randomly choose $N$ points from the Bunny model. And they are centered, scaled in $[-0.5, 0.5]$ to be source point cloud. The target point clouds are generated by randomly rotating the source point cloud. The addition operations of Gaussian noise and outliers are performed in the same way in Section 5.1.

**Methods to Comparision.** Based on the results of comparison in Section 5.1, we choose the Mil to discretize the hemisphere and keep two types of rotation angle estimation. Thus, the following algorithms will be compared:

- *RANSAC*: A classic method using the confidence level of 0.99 as the stopping criterion;
- *GORE* [5]: A guaranteed method that estimates rotation using simple geometric operations and exhaustive sampling;
- *GNC* [13]: A deterministic method based on the graduated non-convexity with truncated least squares costs;
- *BnB* [3]: A global optimal rotation search method using $\pi$-ball as the rotation search space;

**Evaluation Metric.** Following [16], the error between the estimated rotation matrix $\mathbf{R}_{es}$ and the ground-truth $\mathbf{R}_{gt}$ is defined as the geodesic distance

$$e_{\mathbf{R}} = |\arccos\left(\left(trace\left(\mathbf{R}_{gt}^{T}\mathbf{R}_{es}\right) - 1\right)/2\right)| \qquad (2)$$

**Results Analysis.** In this part of experiments, one-to-one correspondences are established using the indexes of points. Figs. 6(a) and 6(b) report the statistics of the results of all methods on the dataset with outlier ratios changing from 15% to 95%. The error of the *GNC* estimator grows rapidly, and it cannot handle the cases whose outlier ratios are higher than 75%. Other methods show good robustness to outliers. However, the runtime of *BnB* is always the highest one, and there is a clear increase for the runtime of *RANSAC* with the increasing outlier ratios. The proposed

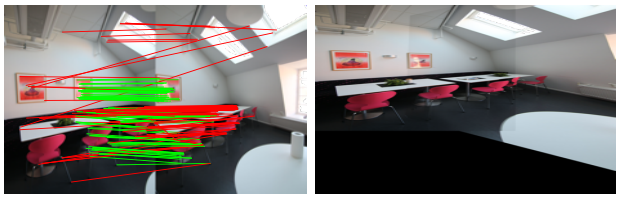

Figure 8. Results of image stitching by RO-DE on PASSTA dataset. The outliers are shown in red.

method achieves the best performance in terms of efficiency while keeping competitive accuracy.

### 5.3. Application: Image Stitching

In this section, we use the PASSTA datasets [10] to test the proposed RO-DE on the application of image stitching. In order to merge a pair of images captured by a rotating camera with known intrinsic $\mathbf{K}$, SURF features are extracted and associated as putative correspondences. In our tests, the rotation $\mathbf{R}$ is estimated by registering the unit-norm vectors back-projected from the homogeneous keypoint coordinates with $\mathbf{K}^{-1}$. Fig. 8 shows the stitching results on the PASSTA datasets, in which the images are assumed to be acquired from a camera fixed on a tripod. The inlier threshold is set as $\xi = 0.02$. All tests terminate in a very short time. Even for 339 pairs with the outlier ratio $83.2\%$ in an example of the Lunch Room dataset, RO-DE can converge in $6.44ms$.

## References


[1] Xuyang Bai, Zixin Luo, Lei Zhou, Hongkai Chen, Lei Li, Zeyu Hu, Hongbo Fu, and Chiew-Lan Tai. Pointdsc: Robust point cloud registration using deep spatial consistency. In *CVPR*.

[2] Jean-Charles Bazin, Yongduek Seo, Richard Hartley, and Marc Pollefeys. Globally optimal inlier set maximization with unknown rotation and focal length. In *ECCV*, pages 803–817, 2014.

[3] Jean-Charles Bazin, Yongduek Seo, and Marc Pollefeys. Globally optimal consensus set maximization through rotation search. In *ACCV*, 2013.

[4] Álvaro Joaquin Parra Bustos, Tat-Jun Chin, and David Suter. Fast rotation search with stereographic projections for 3d registration. In *CVPR*, 2014.

[5] Álvaro Parra Bustos and Tat-Jun Chin. Guaranteed outlier removal for rotation search. In *ICCV*, 2015.

[6] Brian Curless and Marc Levoy. A volumetric method for building complex models from range images. In *SIGGRAPH*, 1996.

[7] Martin A. Fischler and Robert C. Bolles. Random sample consensus: A paradigm for model fitting with applications to image analysis and automated cartography. 1981.

[8] Haoang Li, Ji Zhao, Jean-Charles Bazin, and Yun-Hui Liu. Quasi-globally optimal and near/true real-time vanishing point estimation in manhattan world. *TPAMI*, 2020.

[9] Yinlong Liu, Guang Chen, and Alois Knoll. Globally optimal vertical direction estimation in atlanta world. *TPAMI*, 2020.

[10] Giulia Meneghetti, Martin Danelljan, Michael Felsberg, and Klas Nordberg. Image alignment for panorama stitching in sparsely structured environments. In *Image Analysis*, 2015.

[11] Álvaro Parra Bustos, Tat-Jun Chin, Anders Eriksson, Hongdong Li, and David Suter. Fast rotation search with stereographic projections for 3d registration. *TPAMI*, 2016.

[12] John Parr Snyder. *Map projections–A working manual*, volume 1395. US Government Printing Office, 1987.

[13] Heng Yang, Pasquale Antonante, Vasileios Tzoumas, and Luca Carlone. Graduated non-convexity for robust spatial perception: From non-minimal solvers to global outlier rejection. *RA-L*, 2020.

[14] Heng Yang and Luca Carlone. A quaternion-based certifiably optimal solution to the wahba problem with outliers. In *ICCV*, 2019.

[15] Heng Yang, Jingnan Shi, and Luca Carlone. A polynomial-time solution for robust registration with extreme outlier rates. In *RSS*, 2019.

[16] Heng Yang, Jingnan Shi, and Luca Carlone. Teaser: Fast and certifiable point cloud registration. *IEEE T-RO*, 2021.

[17] Qian-Yi Zhou, Jaesik Park, and Vladlen Koltun. Fast global registration. In *ECCV*, 2016.